Largely Enhanced Photogalvanic Effects in a Phosphorene Photodetector by Strain-Increased Device Asymmetry

Juan Zhao,[1] Yibin Hu,[2] Yiqun Xie,[1,*] Lei Zhang,[3] and Yin Wang[4]

[1] *Department of Physics, Shanghai Normal University, Shanghai 200234, China*

[2] *Shanghai Institute of Technical Physics, Chinese Academy of Sciences, China*

[3] *State Key Laboratory of Quantum Optics and Quantum Optics Devices, Institute of Laser Spectroscopy, and Collaborative Innovation Center of Extreme Optics, Shanxi University, Taiyuan 030006, China*

[4] *Department of Physics and International Centre for Quantum and Molecular Structures, Shanghai University, 99 Shangda Road, Shanghai 200444, China*

(Received 9 August 2020; revised 22 October 2020; accepted 9 November 2020; published 1 December 2020)

The photogalvanic effect (PGE) occurring in noncentrosymmetric materials enables the generation of an open-circuit voltage that is much larger than the bandgap, making it rather attractive in solar cells. However, the magnitude of the PGE photocurrent is usually small, which severely hampers its practical application. Here we propose a mechanism to largely enhance the PGE photocurrent by mechanical strain based on the quantum transport simulations for the two-dimensional nickel-phosphorene-nickel photodetector. A broadband PGE photocurrent governed by the C_s noncentrosymmetry is generated at zero bias under the illumination of linearly polarized light. The photocurrent depends linearly on the device asymmetry, while nonlinearly on the optical absorption. By applying the appropriate mechanical tension stress on the phosphorene, the photocurrent can be substantially enhanced by up to 3 orders of magnitude, which is primarily ascribed to the largely increased device asymmetry. The change in the optical absorption in some cases can also play a critical role in tuning the photocurrent due to the nonlinear dependence. Moreover, the photocurrent can be even further enhanced by mechanical bending, mainly owing to the considerably enhanced device asymmetry. Our results reveal the dependence of the PGE photocurrent on the device asymmetry and absorption in the transport process through a device, and also explore the potential of the PGE in self-powered low-dimensional flexible optoelectronics and low-dimensional photodetections with high photoresponsivity.

DOI: 10.1103/PhysRevApplied.14.064003

I. INTRODUCTION

Optoelectronic properties of two-dimensional (2D) materials have attracted intensive research interest in the past decades for their fascinating potential applications in various fields, including photodetections [1–5], solar cells [6,7] and spintronics [8–10]. There are several light-to-current conversion mechanisms that are usually involved in these 2D optoelectronic devices. The most typical mechanism is the photovoltaic effect that requires the traditional *p-n* junctions to separate the light-induced electron holes. Their efficiency has been improved largely in these years and almost reaches the Shockley-Queisser limitation [11]. The second mechanism is the photoconductor effect, in which the external voltage is necessary for generating the persistent current, yet cannot provide the electrical power generation [12,13]. Other mechanisms like photogating effects are also involved [14–16].

In contrast to these light-to-current conversion mechanisms, the photogalvanic effect (PGE) [17–23], also known as the bulk photovoltaic effect [24–26], enables the generation of the photocurrent without the need for any external voltage or *p-n* junctions, which occur in materials with broken inversion symmetry. The PGE has attracted broad research interest in wide material systems, including the bulk Weyl semimetals [27,28], quantum wells [18], and 2D materials [29]. This mechanism is able to generate an open-circuit voltage that is much larger than the bandgap [25,30], which makes it possible to achieve the light-to-current efficiency exceeding the Shockley-Queisser limit [31]. However, high efficiency has hardly been achieved so far in experiments mainly because of the low magnitude of the PGE photocurrent (photoresponsivity) that is usually less than mA/W. It is therefore rather desirable to find an effective approach to enhance the PGE photocurrent.

Breakthroughs have recently been achieved. It has been demonstrated that the PGE photocurrent obtained in 1D WS_2 nanotubes is several orders of magnitude larger than

*yqxie@shnu.edu.cn

that in flat 2D WS_2 monolayers [6], and that the photoresponsivity is up to 0.1 A/W, which is much larger than PGEs reported in other systems, such as the bulk $BaTiO_3$ [31], TTF-CA [32], and organometallic perovskite halide [33]. This substantially enhanced photocurrent in the 1D WS_2 nanotube has mainly been ascribed to its reduced C_{2nv} or C_{2nh} symmetry, as compared to the 2D WS_2 monolayer (D_{2h}), along with increased optical absorption. These results suggested that reducing the crystal symmetry of a flat 2D semiconducting material by creating a curvature (e.g., bending) can strengthen the PGE and hence enhance the photocurrent. Another important experiment has demonstrated that, by applying an appropriate mechanical stress gradient on the $SrTiO_3$ single crystal, the PGE photocurrent can be enhanced by orders of magnitude [7], which is known as the flexophotovoltaic effect. However, controversy has been raised regarding the fundamental mechanism responsible for this enhancement in the photocurrent [34]. Direct experimental evidence for the effective enhancement of the PGE by mechanical strain has recently been achieved in the Fe-doped $LiNbO_3$ single crystal, in which the photocurrent was increased by 75% even under a tiny uniaxial compressive stress (0.005%) on the lattice [35]. Unfortunately, much higher compressive stress is difficult to achieve experimentally, so further enhancement of the photocurrent has not been investigated. Therefore, it currently remains an open question as to whether the PGE photocurrent can be increased by orders of magnitude under appropriate mechanical stress or bending due to the lack of direct experimental support.

Theoretical studies have revealed that the PGE involves two mechanisms, one of which is connected with the asymmetry in the electron velocity distribution [17,36–38]. Another mechanism stems from the displacement of the electrons in real space when they undergo quantum transitions, namely, shift current [30,36,39–43]. These excellent theoretical studies on the PGE have led to much success in understanding experimental results, and provided deep insights into the physical origin of the PGE [40,44–51]. However, these studies focus mainly on the PGE in periodical systems (crystals), while in practical applications the PGE photocurrent transports through the device that is an open system, and therefore involves statistical and nonequilibrium physics that go beyond the calculations for a periodical system. Therefore, how to enhance the PGE photocurrent flowing through the device under mechanical strain deserves further theoretical investigations.

In this study, we propose a mechanism to enhance the PGE photocurrent generated in the device by quantum transport calculations based on the 2D phosphorene photodetector with nickel electrodes under the vertical illumination of linearly polarized light. A parameter for the device asymmetry is presented, which plays an important role in determining the strength of the PGE. The photocurrent can be substantially enhanced by 3 orders of magnitude by applying the appropriate mechanical tension stress and bending, owing to the largely increased device asymmetry.

II. MODEL AND METHODS

We model a photodetector device with the Ni(100)-phosphorene-Ni(100) configuration, which contains right and left electrodes and the center region, as shown in Figs. 1(a) and 1(b). In the center region of the device, the phosphorene is partially overlapped with Ni(100) electrodes that extend to $y = \pm\infty$, as shown in Fig. 1(b). The lattice constants are $a_x = 3.524$ Å and $a_y = 4.580$ Å for the phosphorene calculated using the VASP code [52,53]. To build a periodic structure, the phosphorene is uniformly stretched by about 6% along the x direction to match the Ni lattice. The Ni electrodes are modeled using five-layer Ni(100) slabs, and the spins of the two ferromagnetic Ni electrodes are set in a parallel configuration. The distance between the phosphorene and the Ni slab surface is 1.95 Å. The phosphorene-Ni(100) contact breaks the intrinsic spacing inversion symmetry of the phosphorene,

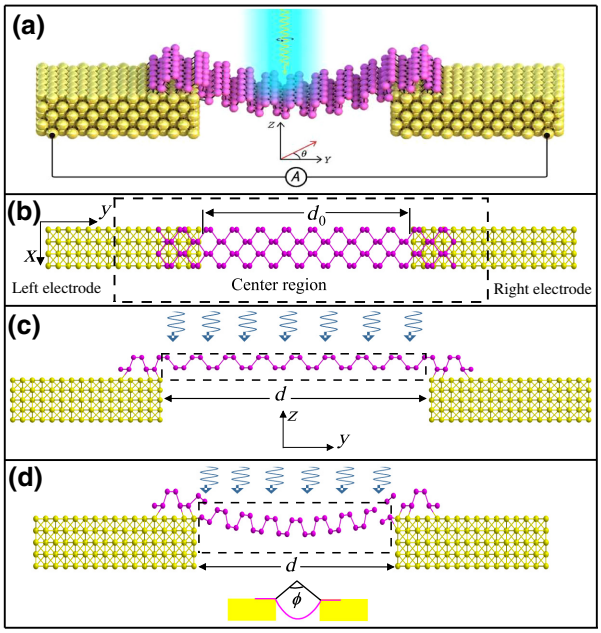

FIG. 1. (a) Illustration of the Ni(100)-phosphorene-Ni(100) photodetector under mechanical bending irradiated by the polarized light. (b) Top view of the device model for the Ni(100)-phosphorene-Ni(100) photodetector without any strains, and side views for the photodetector with (c) tension stress and (d) a bending ratio of 3.9%, which corresponds to a central angle $\phi = 60^\circ$, as indicated in the inset. The d and d_0 denote the distances between the two leads with and without mechanical deformations, respectively. Yellow and pink spheres denote the Ni atoms and P atoms, respectively. The gray wavy lines with arrows denote the incident light irradiated on the free-standing phosphore indicated by the dashed rectangle.

as discussed in our previous work [22]. The whole device structure belongs to the noncentrosymmetric C_s group, which has only one mirror reflection plane located in the y-z plane, considering the periodicity in the x direction. Therefore, the PGE can be induced in the photodetector to generate the photocurrent flowing along the y direction when the free-standing phosphorene in the center region is vertically irradiated by linearly polarized light.

It has been shown that the monolayer phosphorene has an outstanding flexibility under both in-plane and out-of-plane mechanical strains [54–56]. In our simulations, the mechanic tension is applied uniaxially on the phosphorene along the y direction by increasing the y distance d between the two electrodes, and mechanical bending is applied along the out-of-plane direction with a certain central angle ϕ. When mechanical strain is applied, the distance between the two electrodes will change. Accordingly, we can define the ratio for the applied tension stress (ε_y) and bending (ε_b) as $\varepsilon_{y,b} = |(d - d_0)|/d_0 \times 100\%$, where $d_0 = 37.77$ Å when no strain is applied [See Fig. 1(b)]. For example, for bending with a central angle ϕ of 60°, as illustrated in the inset of Fig. 1(d), the bending ratio is 3.9%. The deformed phosphorene is fully relaxed by VASP with the atoms in the Ni electrodes being fixed. In our VASP calculations, the exchange-correlation energy is treated by the projector augmented wave of the Perdew-Burke-Ernzerhof functional [57] with an energy cutoff of 500 eV. The Brillouin zone is sampled with an $8 \times 1 \times 1$ mesh of Monkhorst-Pack k points [58]. A vacuum region of 20 Å in the z direction is added in the 2D supercell to isolate any possible spurious interactions between periodical images of the supercell.

When the center region is irradiated by the polarized light, the photocurrent can be generated. Based on the linear response approximation [59], the photocurrent injecting into the left electrode can be written as [60–62],

$$J_L^{(\mathrm{ph})} = \frac{ie}{h}\int \mathrm{Tr}\{\Gamma_L[G^{<(\mathrm{ph})} + f_L(E)(G^{>(\mathrm{ph})} - G^{<(\mathrm{ph})})]\}dE, \tag{1}$$

where $G^{>[<(\mathrm{ph})]}(E)$ is the greater (lesser) Green's function including electron-photon interactions, and f_L is the Fermi-Dirac distribution function. To analyze the PGE, we assume that the temperature is low enough and hence the Fermi function f_L is stepwise, so that Eq. (1) can be rewritten as [63]

$$\begin{aligned} J_L^{(\mathrm{ph})} &= \frac{ie}{h}\int_{-\infty}^{0} \mathrm{Tr}[\Gamma_L G^{>(\mathrm{ph})}]dE + \frac{ie}{h}\int_{0}^{+\infty} \mathrm{Tr}[\Gamma_L G^{<(\mathrm{ph})}]dE \\ &= J_- + J_+, \end{aligned} \tag{2}$$

where $J_- = (ie/h)\int_{-\infty}^{0} \mathrm{Tr}[\Gamma_L G^{>(\mathrm{ph})}]dE < 0$ denotes the current flowing out of the center region to the left lead, while $J_+ = (ie/h)\int_{0}^{+\infty} \mathrm{Tr}[\Gamma_L G^{<(\mathrm{ph})}]dE > 0$ denotes the current flowing into the center region from the lead. The magnitude of the PGE photocurrent is thus determined by $|J_L^{(\mathrm{ph})}| = \Delta J = |J_+ - |J_-||$. Therefore, we can define a factor A to describe the device asymmetry as

$$A = \left|\frac{J_+ - |J_-|}{J_+}\right|. \tag{3}$$

For the device with space inversion symmetry, the current flowing into the center region equals that which flows out of the center region, that is, there is no net current flowing through the device. In this case, $J_+ = |J_-|$, so $J_L^{(\mathrm{ph})} = 0$, and $A = 0$. For the device without inversion symmetry, there is a net photocurrent and A is nonzero. The magnitude of the photocurrent can then be rewritten as

$$|J_L^{(\mathrm{ph})}| = AJ_+. \tag{4}$$

Note that J_+ includes $\Gamma_L G^{<(\mathrm{ph})}$, while $G^{<(\mathrm{ph})}$ includes the photon propagator $D^<$ [59],

$$D^<_{ln;qm}(E) = 2\pi M_{ln} M_{qm} N \delta(E - \hbar\omega), \tag{5}$$

where

$$M_{ln} = \frac{e}{m}\left(\frac{\hbar\sqrt{\tilde{\mu}_r\tilde{\epsilon}_r}I_\omega}{2N\omega\tilde{\epsilon}c}\right)^{1/2}\langle l|\mathbf{p}\cdot\mathbf{e}|n\rangle. \tag{6}$$

Here, l, n, m, q are atomic orbital labels, I_ω is the photon flux, m_0 is the bare electron mass, e is the electronic charge, $\tilde{\mu}_r$ is the relative magnetic susceptibility, $\tilde{\epsilon}_r$ is the relative dielectric constant and $\tilde{\epsilon}$ the static dielectric constant, $\mathbf{p}$ is the electron momentum, and $\mathbf{e}$ is the light polarization vector. Therefore, in essentials the photon propagator $D^<$ corresponds to the excitation of an electron by the absorption of a photon [59,64]. As a comparison, we give the optical absorption coefficient α of a material [24,65],

$$\begin{aligned} \alpha(\omega) = \frac{e^2}{2\pi^2\epsilon_0 m_0^2\omega c}\sum_{n,l}\int (f_n - f_l)|\langle \mathbf{k}, l|\mathbf{p}\cdot\mathbf{e}|\mathbf{k}, n\rangle|^2 \\ \times \delta(E_l - E_n - \hbar\omega)d^3k. \end{aligned} \tag{7}$$

It can be seen that the photon propagator $D^<$ and the optical absorption coefficient α have the same physical meaning, that is, the excitation of electrons by absorbing the photon energy of $\hbar\omega$. This indicates that J_+ should have a nonlinear dependence on the optical absorption of the device due to the tensor product of $D^<$ with the coupling matrix Γ. Consequently, the photocurrent $J_L^{(\mathrm{ph})}$ has a linear dependence on the device asymmetry A (a scalar), while a nonlinear dependence on the optical absorption of the device, according to Eq. (4).

The PGE photocurrent also varies with the light polarization. In our previous work, we showed that, for linearly polarized light, the photocurrent has a dependence on the polarization angle θ and can be written as [22,61,66]

$$J_L^{(\mathrm{ph})} = \frac{ie}{h}\int (\cos^2\theta \mathrm{Tr}\{\Gamma_L[G_1^{<(\mathrm{ph})} + f_L(G_1^{>(\mathrm{ph})} - G_1^{<(\mathrm{ph})})]\} + \sin^2\theta \mathrm{Tr}\{\Gamma_L[G_2^{<(\mathrm{ph})} + f_L(G_2^{>(\mathrm{ph})} - G_2^{<(\mathrm{ph})})]\} + 2\sin(2\theta)\mathrm{Tr}\{\Gamma_L[G_3^{<(\mathrm{ph})} + f_L(G_3^{>(\mathrm{ph})} - G_3^{<(\mathrm{ph})})]\})dE,$$

where $G_{1,2,3}^{>[<(\mathrm{ph})]}$ depends on the photon frequency ω, the electron momentum $\mathbf{p}$, and the polarization vector $\mathbf{e}$=cos $\theta\mathbf{e}_1$+sin $\theta\mathbf{e}_2$. In our calculations, the unit vectors $\mathbf{e}_1$ and $\mathbf{e}_2$ are set along the x (zigzag) and y (armchair) directions, respectively. It is worth noting that the photocurrent is proportional to the photon flux I_ω, and is thus proportional to the light power, within the linear response approximation [59]. The photocurrent can be further normalized as $J = J_L^{(\mathrm{ph})}/eI_\omega$. Note that the normalized photocurrent J still has a dimension of area, i.e., a_0^2/photon, where a_0 is the Bohr radius. To facilitate the analysis of the enhancement of the photocurrent, we define three factors, namely, R_J, R_A, and R_α, which respectively denote the increase ratio of the photocurrent J, device asymmetry A, and the optical absorption coefficient α with respect to that when no strain is applied.

III. RESULTS AND DISCUSSION

We calculate the PGE photocurrent under different mechanical stress for the Ni-phosphorene-Ni photodetector. The photon energy considered is from 1.2 to 3.2 eV, which is larger than the bandgap of the pristine phosphorene and covers the near infrared and visible range. We find that the photocurrent J shows the cosine dependence on the polarization angle θ for all of the photon energies, which is a characteristic behavior of the PGE photocurrent governed by the C_s symmetry [17]. Examples are presented in Fig. 2(a) for photon energies 1.5, 1.6, and 1.7 eV, when no mechanical tension is applied. Specifically, the photocurrent for a photon energy of 1.5 eV is well fitted by the function $0.017\cos(2\theta) + 0.018$, which agrees qualitatively with the phenomenological theory [17,18].

We then examined the effect of mechanical strain on the behavior of the photocurrent, finding that the photocurrent still preserves the cosine dependence on the 2θ under mechanical tension, since the mechanical tension applied uniformly along the y direction does not change the C_s symmetry. Examples are shown in Fig. 2(b) for a tension ratio of $\varepsilon_y = 30\%$. However, it can be seen that the magnitude of the photocurrent can be much larger than that without mechanical tension. For comparison, we obtained

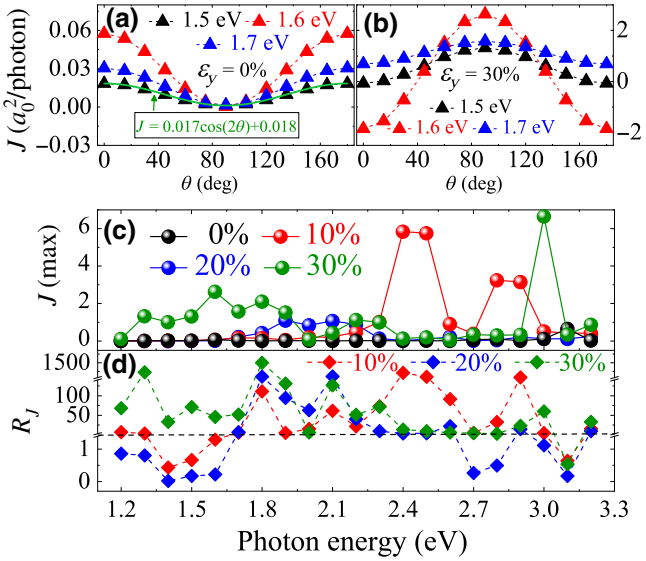

FIG. 2. The photocurrent J for photon energies 1.5, 1.6, and 1.7 eV without (a) and with (b) mechanical tension, where the green solid line denotes the fitting function. (c) The variation of the maximum J with photon energy for different tension ratios ε_y. (d) The increase ratio R_J of the photocurrent under the different mechanical tensions with respect to that without mechanical tensions.

the maximum photocurrent at $\theta = 90^\circ$ or 0° for all of the photon energies under the different tension ratios, as shown in Fig. 2(c). It can be seen that the magnitude of the photocurrent is substantially enhanced by mechanical tension for most of the photon energy from 1.2 to 3.2 eV. More specifically, in Fig. 2(d) we present the increase ratio R_J of the photocurrent under mechanical tension with respect to that without mechanical tension. Noticeably, at $\varepsilon_y = 30\%$, R_J is greater than 1 for almost all of the photon energies except 3.1 eV (see the green squares), and R_J exceeds 10^2 for a number of photon energies. Moreover, the maximum ratio reaches 1.5×10^3 for $\varepsilon_y = 30\%$ at a photon energy of 1.8 eV. For the other ε_y, R_J is also greater than 1 for most of the photon energies.

To understand this remarkable enhancement of the photocurrent under mechanical tension, we first analyze the device asymmetry A and examine its behavior for different tension ratios ε_y. The asymmetry A is determined by the photon energy and also the tension ratio. We mainly focus on the photon energies 2.9, 2.5, and 1.8 eV, where the PGE photocurrent is enhanced the most. The A under different ε_y and its increase ratio R_A are calculated for $\varepsilon_y =$ 5%, 10%, 12.5%, 15%, 17.5%, 20%, and 30% with respect to those without tension stress. In Figs. 3(a), 3(c), and 3(e) we show the variation of R_A (black stars) and R_J (green squares) with ε_y for photon energies 2.9, 2.5, and 1.8 eV, respectively, and in Figs. 3(b), 3(d), and 3(f) we give the normalized ratios with respect to their largest value. From the normalized ratios, we observe that the overall trend of

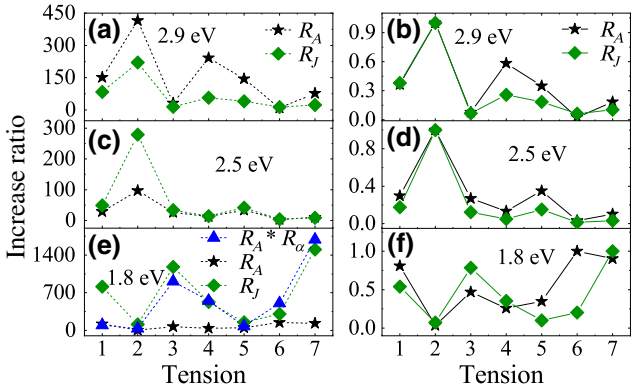

FIG. 3. The increase ratios of the device asymmetry (R_A) and of the photocurrent (R_J) at different tension ratios $\varepsilon_y =$ (1) 5%, (2) 10%, (3) 12.5%, (4) 15%, (5) 17.5%, (6) 20%, (7)30% for photon energies (a),(b) 2.9 eV, (c),(d) 2.5 eV, and (e),(f) 1.8 eV, with normalized ratios plotted in (b),(d),(f).

R_J matches monotonously with that of R_A for different ε_y. This indicates that the enhancement of the PGE photocurrent is primarily determined by the change in the device asymmetry A. Nevertheless, there are evident differences between R_A and R_J at some ε_y, as shown in Figs. 3(a), 3(c), and 3(e). This means that the enhancement of the photocurrent cannot be exclusively attributed to the change in A. The influences from the change in the optical absorption induced by the mechanical tension should also be considered. Therefore, we calculated the optical absorption coefficient α of the monolayer phosphorene and the increase ratio R_α under the different ε_y, as listed in Table I. Here, we calculated the optical absorption coefficient α based on the 2D monolayer phosphorene, which is an acceptable approximation according to the analysis below.

According to Eq. (4), in general, the photocurrent should have a nonlinear dependence on the optical absorption. This nonlinear relationship is difficult to express explicitly due to the tensor product of Γ and $G^{<\mathrm{ph}}$, which varies with the different photon energies and mechanical strain. For example, for a photon energy of 2.5 eV [Fig. 3(c)], the change in the optical absorption seems to have a negligible influence on the photocurrent since R_A almost equals R_J for most of the ε_y values except $\varepsilon_y = 10\%$ (2). In contrast, R_A is evidently less than R_J for a photon energy of 1.8 eV [Fig. 3(e)], which indicates a different dependence on the optical absorption. Interestingly, we find that at most of the ε_y values $R_J \approx R_A * R_\alpha$, as the blue triangles in Fig. 3(e) shows. This indicates that, for a photon energy of 1.8 eV, the photocurrent has a linear dependence on both the optical absorption and the asymmetry A in most of the cases. Besides, Fig. 3(e) indicates that, at $\varepsilon_y = 12.5\%$ and 30%, R_α has the largest contribution to the increase of the photocurrent (R_J), as compared with those at the other ε_y. Moreover, we find that R_α has the large values of 13.191 and 12.644 at $\varepsilon_y = 12.5\%$ and 30% (Table I), respectively. To understand this large increase in the optical absorption for a photon energy of 1.8 eV at $\varepsilon_y = 12.5\%$ and 30%, in Fig. 4(a) we show how the optical absorption α varies with photon energy. Here, at $\varepsilon_y = 12.5\%$, α is given for light polarization along the y direction ($\theta = 0^\circ$), while at $\varepsilon_y = 30\%$ and 0%, α is given for polarization along the x direction ($\theta = 90^\circ$), at which the largest photocurrent is achieved for these ε_y. The α for x polarization at $\varepsilon_y = 0\%$ is obviously smaller than that in the y direction at $\varepsilon_y = 12.5\%$ for a photon energy less than 2.8 eV, which

TABLE I. The optical absorption coefficient α and its increase ratio R_α of the monolayer phosphorene under mechanical tension stress and bending. The "x" and "y" denote the polarization directions for $\theta = 90^\circ$ and 0°, respectively, at which the largest photocurrent is achieved.

		ε_y							
Tension (eV)		0%	5%	10%	12.5%	15%	17.5%	20%	30%
1.8	α	0.344(x)	0.274(x)	2.286(y)	4.536(y)	5.034(y)	0.510(x)	1.177(x)	4.348(x)
	R_α		0.798	6.648	13.191	14.639	1.483	3.424	12.644
2.5	α	1.521(x)	1.892(x)	3.651(x)	5.073(x)	5.558(x)	4.046(x)	6.410(x)	6.246(y)
	R_α		1.243	2.400	3.334	3.652	2.659	4.213	4.105
2.9	α	4.585(x)	4.142(x)	5.469(x)	3.267(x)	1.927(y)	2.077(x)	8.390(x)	5.248(y)
	R_α		0.903	1.193	0.713	0.420	0.453	1.830	1.145
		ε_b							
Bending (eV)		0%	0.9%	1.3%	2.5%	3.9%	5.3%	6.3%	8%
1.3	α	0.066(x)	1.482(y)	1.500(y)	1.639(y)	1.634(y)	1.661(y)	1.917(y)	0.459(x)
	R_α		22.390	22.663	24.773	24.699	25.109	28.976	6.943
1.8	α	0.180(x)	1.965(y)	1.980(y)	1.999(y)	2.010(y)	2.044(y)	2.017(y)	2.165(y)
	R_α		10.902	10.982	11.090	11.150	11.340	11.188	12.010
2.1	α	1.157(y)	1.474(x)	1.761(y)	1.705(y)	1.369(x)	1.308(x)	1.657(y)	2.311(y)
	R_α		1.273	1.522	1.473	1.183	1.130	1.432	1.996

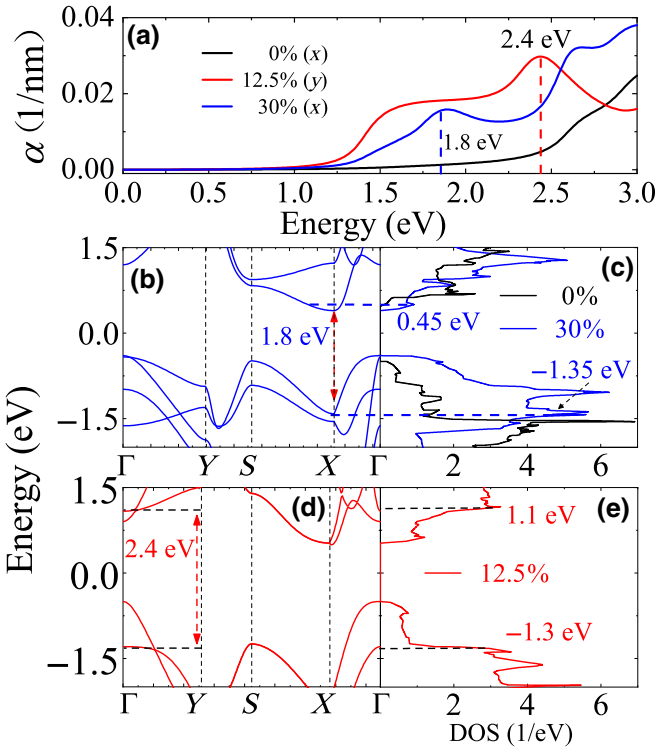

FIG. 4. (a) The optical absorption coefficient α of the 2D monolayer phosphorene at $\varepsilon_y = 30\%$ and 0% for the light polarized along the x direction, and at $\varepsilon_y = 12.5\%$ for the light polarized along the y direction. Panels (b) and (c) show the electronic bandstructure and density of states (DOS) for $\varepsilon_y = 30\%$ (blue lines), with the DOS at $\varepsilon_y = 0\%$ (solid black line) also shown. Panels (d) and (e) show the electronic bandstructure and DOS at $\varepsilon_y = 12.5\%$, where $E = 0$ eV corresponds to the Fermi energy. The double-headed arrows indicate photoexcited electron transitions.

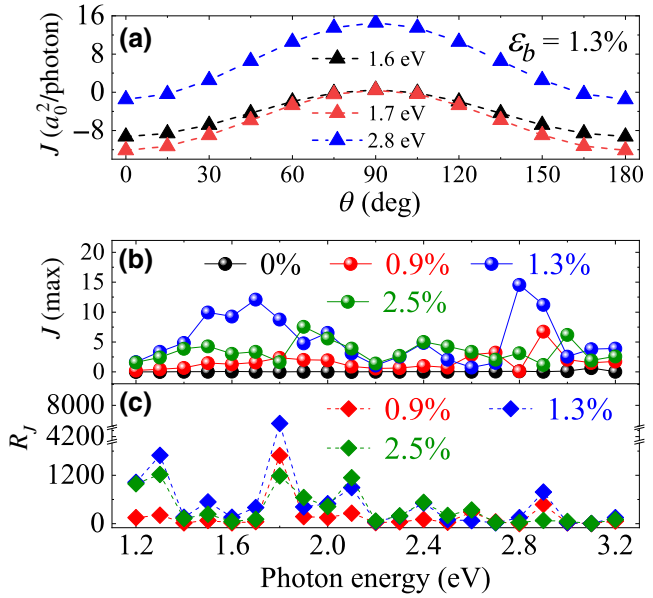

FIG. 5. (a) The photocurrent for photon energies 1.5, 1.6, and 1.7 eV under mechanical bending. (b) The variation of the maximum photocurrent with photon energy under the different bending ratios ε_b. (c) The increase ratio R_J of the photocurrent under the different mechanical tensions.

can be attributed to the anisotropic optical absorption of the phosphorene, as has been revealed both in experiments [67] and theory [68,69]. It can also be seen that there are evident absorption peaks located around 1.8 and 2.4 eV for $\varepsilon_y = 30\%$ and 12.5%, respectively. In Fig. 4(c) we show that there are two peaks in the DOS located at $+0.45$ and -1.35 eV for $\varepsilon_y = 30\%$, which corresponds to the first conduction and valence bands around the "X" point in the first Brillouin zone, respectively [Fig. 4(b)]. According to Fermi's golden rule, the probability of electron transitions is proportional to the DOS. This means that the probability of electron transitions between these two density-of-state peaks within the first valence and conduction bands is larger, and therefore leads to the optical absorption peak for a photon energy of 1.8 eV. Moreover, the DOS at $\varepsilon_y = 30\%$ is overall larger than that at $\varepsilon_y = 0\%$ (black line), as shown in Fig. 4(c), and therefore the absorption is largely increased. Similarly, the optical absorption peak located at 2.4 eV for $\varepsilon_y = 12.5\%$ can be mainly attributed to electron transitions between the energy levels $+1.1$ and -1.3 eV, corresponding to the second valence and conduction bands at the "Γ" point, where the sharp DOS peak appears, as indicated in Figs. 4(d) and 4(e)

We next consider the influence on the photocurrent of applying mechanical bending on the free-standing part of the phosphorene, as shown in Fig. 1(d). Obviously, the space inversion symmetry of the phosphorene is broken by the bending, while the whole device still remains in C_s symmetry. Note that the mechanical tension does not change the symmetry of the phosphorenene. This means that the asymmetry of the device can be further increased by mechanical bending, and therefore the PGE photocurrent would be enhanced further, as compared with that under mechanical tension stress. We find that the photocurrent still holds the form $\cos(2\theta)$ due to the unchanged C_s symmetry of the device, as illustrated in Fig. 5(a). Evidently, the magnitude of the photocurrent is largely increased, as compared to that without mechanical bending, as shown in Fig. 5(b). Moreover, the maximum photocurrent is 14.5 at 2.8 eV for $\varepsilon_b = 1.3\%$, which is 2 times larger than that (6.6) under tension stress [see Fig. 2(c)].

We observe that, for a number of photon energies, R_J is greater than 10^3, and that the maximum R_J reaches about 6.26×10^3 for a photon energy of 1.8 eV at $\varepsilon_b = 1.3\%$ (blue squares), which is about 4 times larger than that under mechanical tension. At photon energies of 1.3, 1.8, and 2.1 eV, the photocurrent shows the largest enhancement. We therefore present in Figs. 6(a), 6(c), and 6(e) R_A and R_J for these photon energies at different mechanical bending ratios $\varepsilon_b =$

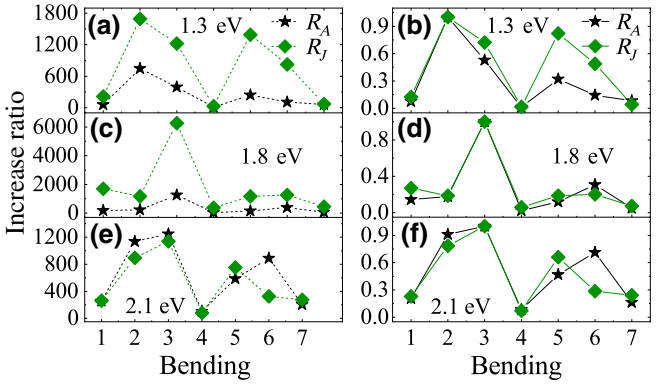

FIG. 6. The increase ratios of the device asymmetry (R_A) and of the photocurrent (R_J) at different bending ratios $\varepsilon_b =$ (1) 0.9%, (2) 1.3%, (3) 2.5%, (4) 3.9%, (5) 5.3%, (6) 6.3%, (7) 8% for photon energies (a),(b) 1.3 eV, (c),(d) 1.8 eV, and (e),(f) 2.1 eV, with normalized ratios plotted in (b),(d),(f).

(1) 0.9%, (2) 1.3%, (3) 2.5%, (4) 3.9%, (5) 5.3%, (6) 6.3%, and (7) 8%, and correspondingly present in Figs. 6(b), 6(d), and 6(f) the normalized ratios. It can be seen that the trend of R_J is in good agreement with that of R_A. This indicates that the remarkable enhancement of the photocurrent should also be mainly attributed to the increased device asymmetry A. Nevertheless, the magnitude of R_A still differs from R_J. For photon energies 1.3 and 1.8 eV, R_A is evidently less than R_J at the different ε_b, as shown in Figs. 6(a) and 6(c). Therefore, we should consider the influence of the change in the optical absorption. We find that the optical absorptions are overall increased evidently at the different ε_b for photon energies 1.8 and 1.3 eV, as listed in Table I. This means that the photocurrent has a positive dependence on the optical absorption. In contrast, for a photon energy of 2.1 eV, R_A has a much smaller deviation from R_J [Fig. 6(c)], which indicates that the change in the optical absorption has a very small influence on the photocurrent. Accordingly, we find that $1 < R_\alpha < 2.0$ at every ε_b, which means that the optical absorption changes slightly under mechanical bending for a photon energy of 2.1 eV. Besides, it is worth noting that, under mechanical bending, the largest R_A is 1254 at ε_b=2.5% for a photon energy of 1.8 eV [see Fig. 6(c)], while the largest R_A is 415 achieved under a mechanical tension stress of $\varepsilon_y = 10\%$ for 2.9 eV [see Figs. 3(a)]. This means that the device asymmetry is indeed further strengthened by mechanical bending since it breaks the inversion symmetry of the phosphorene, while mechanical tension stress does not.

We find that, under mechanical bending stress, α is enhanced for a photon energy below 3.0 eV. Examples are given in Fig. 7(a) for $\varepsilon_b = 0.9\%$ and 3.9%, showing that α at different ε_b has a similar trend varies similarly for increasing photon energies, and so does the DOS [Fig. 7(b)]. From about a photon energy of 1.5 eV, α reaches a larger value and is evidently greater than that

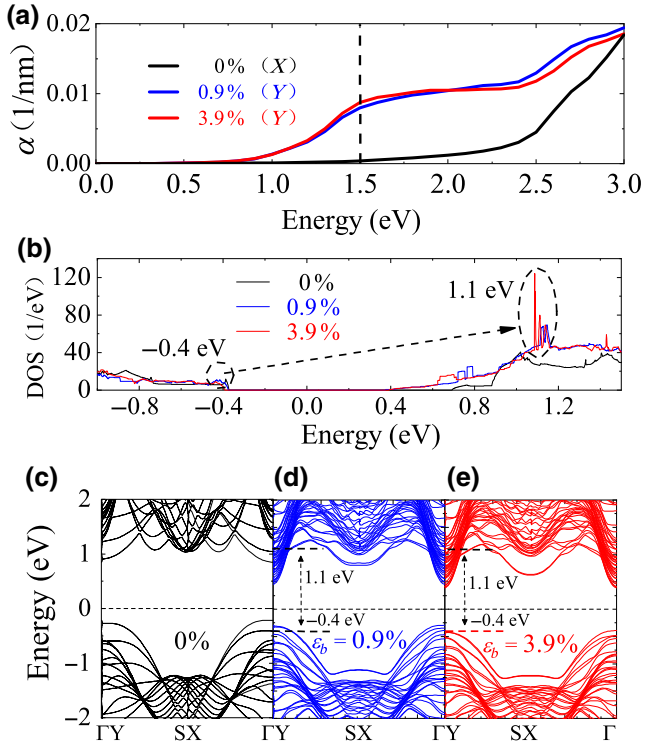

FIG. 7. The optical absorption (a) and the DOS (b) at different bending ratios ε_b. Panels (c)–(e) show the electronic bandstructure for $\varepsilon_b = 0\%, 0.9\%$, and 3.9%, respectively. The double-headed arrows indicate photoexcited electron transitions between the valance and conduction bands, corresponding to the density-of-state peaks indicated in (b).

without mechanical bending. Correspondingly, we observe sharp density-of-state peaks around −0.4 and +1.1 eV, as shown in Fig. 7(b), and, moreover, the DOS in the conduction bands is evidently larger than that without mechanical bending. The increased DOS is attributed to the increased density of the energy bands in the conduction bands around the Γ point, induced by mechanical bending, as shown in Figs. 7(d) and 7(e). Therefore, a larger electron transition probability between the corresponding energy levels, as indicated in the Fig. 7(d), will lead to the enhanced α.

We note that there is a prestretch (about 6%) in the phosphorene along the x direction before applying mechanical bending in order to match the lattice of the underlying Ni(100) surface, and for every bending ratio, this prestretch is invariant. This x-direction stretch should also have an influence on the photocurrent. However, we have shown that, under different bending ratios, the photocurrent can be largely enhanced, as compared to that without bending (i.e., only with the prestretch in the x direction). This means that the prestretch in the x direction by itself cannot lead to an appreciable enhancement in the photocurrent.

We now show that the large enhancement of the PGE photocurrent under the appropriate mechanical strain is primarily due to the substantially increased device

asymmetry, while the change in the optical absorption has a weaker contribution to the enhancement in most of the cases. This point is in agreement with recent experimental findings, which showed that the change in the asymmetry of the $LiNbO_3$ single crystal by mechanical compressive stress has a more important contribution on the enhancement of the PGE photocurrent than the change in the optical absorption [35]. Our results show that, under an appropriate mechanical stress, the PGE photocurrent can be substantially enhanced by up to 3 orders of magnitude. In this regard, it is understandable that in the flexophotovoltaic effect the mechanical gradient can induce a considerable enhancement of the PGE photocurrent for the $SrTiO_3$ single crystals [7]. Moreover, in our work the mechanical bending is even more effective in improving the PGE photocurrent, which is in good agreement with the essential point derived from the recent experiments that reducing the structure symmetry can largely enhance the PGE photocurrent in WS_2 nanotubes [6]. Interestingly, recent experiments have also shown that the photocurrent generated in the flexible 2D $PtSe_2$ phototransistor [70] and the 2D antimonene photodetector [71] can be enhanced by mechanical bending, which suggests that the mechanical-tuned PGE may play a role.

To give further insight into the experiments regarding the large enhancement of the PGE in WS_2 nanotubes [6], we simulate the PGE in the (18,0) phosphorene nanotube with the zigzag edge [72], as shown in Fig. 8. This nanotube has an indirect bandgap of 0.66 eV [Fig. 8(c)], with the noncentrosymmetric D_{2d} symmetry. The center region of the nanotube is illuminated by linearly polarized light with a photon energy from 1.0 to 3.2 eV. For comparison, the number of illuminated phosphorene atoms is 28, which is the same as that illuminated in the Ni(100)-phosphorene photodetector. In Fig. 8(d) we show that the generated PGE photocurrent varies in the form $\cos(2\theta + \theta_0)$, where θ_0 is a phase shift determined by the photon energy and the asymmetry of the illuminated area (atoms). The photocurrent of this zigzag phosphorene nanotube can be much larger than that of the Ni(100)-phosphorene photodetector without mechanical stress. The increase ratio R_J is presented in Fig. 8(e). The largest R_J is up to 1.1×10^3 for a photon energy of 1.0 eV, and for several photon energies, R_J is of the order of 10^2; moreover, for most of the photon energies, R_J is greater than 1 except at 3.1 eV. This result shows that the large enhancement of the PGE photocurrent can be achieved by using a nanotube with appropriate symmetry.

It is worth noting that there are some limitations in our calculations. The first limitation is that the phosphorene in the photodetector is only about 4 nm along the transport direction, which is much shorter than that used in real experiments. However, our results can be generalized qualitatively to the photodetector with much larger size, e.g., of micrometers. The reason is that the PGE is determined by the symmetry of the system, and the PGE

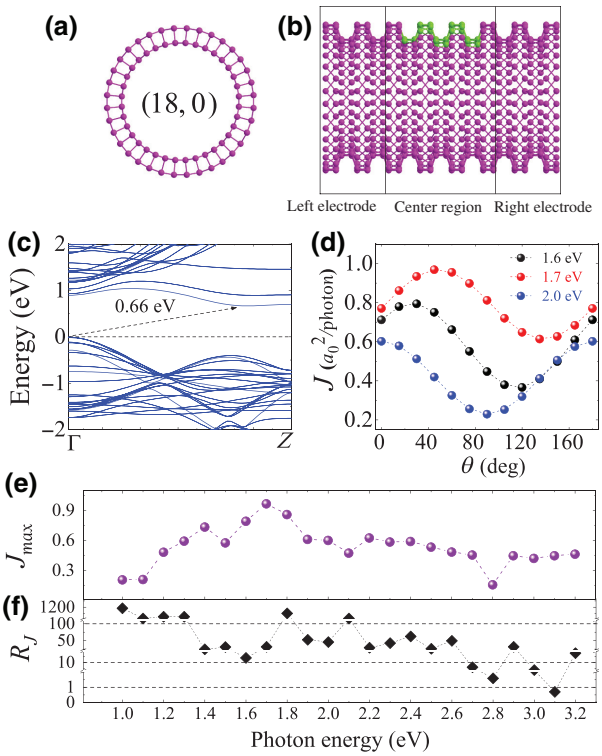

FIG. 8. (a) The cross-sectional view of the (18,0) phosphorene nanotube with the zigzag edge. (b) The device model for the photocurrent calculation, where the green atoms are those illuminated by linearly polarized light. (c) The electronic bandstructure of the (18,0) phosphorene nanotube with an indirect bandgap of 0.66 eV. (d) The PGE photocurrent for photon energies 1.6, 1.7, and 2.0 eV. (e) The maximum photocurrent $J_{\max}$ and (f) the increase ratio R_J with respect to the photocurrent of the Ni(100)-phosphorene-Ni(100) photodetector without any mechanical stress.

photocurrent is proportional to the photon flux based on linear response theory [59]. Therefore, enlarging the size (area) of the phophorene will increase the magnitude of the photocurrent, while not changing its qualitative behavior. For example, the photocurrent will always keep the cosine dependence on the polarization angle θ, as long as the C_s symmetry in the photodetector is preserved. The second limitation is that, due to the limited length in our model, the phosphorene in the center region of the photodetector is a nanoribbon with the zigzag edge, while we treat it as the 2D monolayer phosphorene for the analysis of the change in the optical absorption under various mechanical strains. The reasons are as follows. Firstly, the Ni-phosphorene contact has a strong interaction, which saturates the dangle bonds in the zigzag edge of the phosphorene nanoribbon. In this case, it is very difficult to determine the accurate edge states, and therefore the exact model for calculating the optical absorption of the phosphorene nanoribbon in such cases is difficult to be achieved. Secondly, the optical absorption of the phosphorene is anisotropic between the zigzag and armchair directions. Based on the

2D phosphorene, the influence of the anisotropic optical absorption on the PGE photocurrent is examined by analyzing the photoexcited interband transitions for the light polarization along both the zigzag and armchair direction, whereas for the nanoribbon, only one direction can be considered. Thirdly, the large enhancement of the PGE photocurrent is mainly due to the increased device asymmetry, while the optical absorption has less contributions in most of the cases. For these reasons, we analyze the optical absorption of the phosphorene in the photodetector based on the 2D phosphorene, which is an approximation, yet an acceptable compromise. In addition, there can be an interesting quantum size effect on the energy level of the phosphorene nanoribbon, which can largely enhance the optical absorption, as has been proposed recently in theory for the graphene nanoribbon [73]. However, in our model this effect is severely suppressed since the edge boundary conditions are changed due to the strong interactions between the phosphorene and the underlying Ni(100) surface.

In this work, the PGE photocurrent is spin polarized due to the spin injection from the ferromagnetic Ni electrodes. It is well known that there is a conductivity mismatch in the partial contact between the metal electrodes and 2D materials, as has been revealed in the Ni-graphene contact [74] and the metal-transition metal disulfide contacts [75]. In our Ni-phosphorene contact, the spin conductivity of the monolayer phosphorene differs from the Ni electrodes, and therefore causes significant backscattering of electrons in the Ni-phosphorene interface, and then leads to low spin injection efficiency (SIE). A relatively low SIE of around 60% was found in our previous study for the Ni-phosphorene-Ni magnetic junctions [76,77]. In this work, the SIE of the photocurrent can be tuned by the mechanical strains. The reason is that the mechanical strains change the orbital overlap, and the tunnel barrier between the Ni surface and the covered phosphorene, as well as the Schottky barrier between the Ni-phosphorene contact and the free-standing phosphorene, and therefore change the conductivity mismatch between the conduction channels of the phosphorene and those of the Ni electrodes. However, we do not intent to give a detailed discussion on the SIE in the present work, as we mainly focus on the enhancement of the magnitude of the photocurrent.

IV. CONCLUSIONS

In summary, we have investigated the large enhancement of the PGE in the nickel-phosphorene-nickel photodetector tuned by mechanical tension and bending, using the quantum transport calculations. The photocurrent can be substantially improved by 3 orders of magnitude by applying the appropriate mechanical tension and bending. The remarkable enhancement of the photocurrent is overall mainly due to the largely increased device asymmetry, although the change in the optical absorption can also play an important role in some cases. Mechanical bending can enhance the photocurrent more effectively than the tension stress, since it breaks the inversion symmetry of the phosphorene and hence largely strengthens the device asymmetry. Moreover, the PGE photocurrent of the phosphorene nanotube with the appropriate symmetry can also be much larger than the photodetector without mechanical strain. Our results propose an approach to largely enhance the PGE photocurrent by applying mechanical tension and bending, and shed light on applications of the PGE in low-power 2D flexible optoelectronics and low-dimensional photodetections with high photoresponsivity, as well as give insights into the enhancement of the PGE achieved recently in experiments on nanotubes and flexophotovoltaic effects.

ACKNOWLEDGMENT

This work is supported by the National Natural Science Foundation of China under Grants No. 51871156, No. 11704232 and No. 12074230, the National Key R&D Program of China under Grants No. 2017YFA0304203 and No. 1331KSC, and the Shanxi Province 100-Plan Talent Program.

[1] M. Long, P. Wang, H. Fang, and W. Hu, Progress, challenges, and opportunities for 2D material based photodetectors, Adv. Funct. Mater. **29**, 1803807 (2019).

[2] N. Huo and G. Konstantatos, Recent progress and future prospects of 2D-based photodetectors, Adv. Mater. **30**, 1801164 (2018).

[3] H. Luo, B. Wang, E. Wang, X. Wang, Y. Sun, Q. Li, S. Fan, C. Cheng, and K. Liu, Phase-transition modulated, high-performance dual-mode photodetectors based on WSe_2/VO_2 heterojunctions, Appl. Phys. Rev. **6**, 041407 (2019).

[4] A. Rogalski, M. Kopytko, and P. Martyniuk, Two-dimensional infrared and terahertz detectors: Outlook and status, Appl. Phys. Rev. **6**, 021316 (2019).

[5] D. Wu, J. Guo, J. Du, C. Xia, L. Zeng, Y. Tian, Z. Shi, Y. Tian, X. J. Li, Y. H. Tsang, and J. Jie, Highly polarization-sensitive, broadband, self-powered photodetector based on graphene/PdSe2/Germanium heterojunction, ACS Nano **13**, 9907 (2019).

[6] Y. J. Zhang, T. Ideue, M. Onga, F. Qin, R. Suzuki, A. Zak, R. Tenne, J. H. Smet, and Y. Iwasa, Enhanced intrinsic photovoltaic effect in tungsten disulfide nanotubes, Nature **570**, 349 (2019).

[7] M.-M. Yang, D. J. Kim, and M. Alexe, Flexo-photovoltaic effect, Science **360**, 904 (2018).

[8] J. Kim, K. W. Kim, D. Shin, S. H. Lee, J. Sinova, N. Park, and H. Jin, Prediction of ferroelectricity-driven Berry curvature enabling charge- and spin-controllable photocurrent in tin telluride monolayers, Nat. Commun. **10**, 3965 (2019).

[9] L. Xie and X. Cui, Manipulating spin-polarized photocurrents in 2D transition metal dichalcogenides, PNAS **113**, 3746 (2016).

[10] S. Zamani and R. Farghadan, Graphene Nanoribbon Spin-Photodetector, Phys. Rev. Appl. **10**, 034059 (2018).

[11] W. Shockley, The theory of pn junctions in semiconductors and pn junction transistors, ATT Tech. J. **28**, 435 (1949).

[12] H. Huang, J. Wang, W. Hu, L. Liao, P. Wang, X. Wang, F. Gong, Y. Chen, G. Wu, W. Luo, H. Shen, T. Lin, J. Sun, X. Meng, X. Chen, and J. Chu, Highly sensitive visible to infrared $MoTe_2$ photodetectors enhanced by the photogating effect, Nanotechnology **27**, 445201 (2016).

[13] M. M. Furchi, D. K. Polyushkin, A. Pospischil, and T. Mueller, Mechanisms of photoconductivity in atomically thin MoS2, Nano Lett. **14**, 6165 (2014).

[14] H. Wang, C. Cheng, L. Zhang, H. T. Liu, Y. Zhao, Y. L. Guo, W. P. Hu, G. Yu, and Y. Liu, Inkjet printing short-channel polymer transistors with high-performance and ultrahigh photoresponsivity, Adv. Mater. **26**, 4683 (2014).

[15] C. Qian, J. Sun, L.-A. Kong, G. Gou, M. Zhu, Y. Yuan, H. Huang, Y. Gao, and J. Yang, High-performance organic heterojunction phototransistors based on highly ordered copper phthalocyanine/para-sexiphenyl thin films, Adv. Funct. Mater. **27**, 1604933 (2017).

[16] M. Cao, C. Zhang, Z. Cai, C. Xiao, X. Chen, K. Yi, Y. Yang, Y. Lu, and D. Wei, Enhanced photoelectrical response of thermodynamically epitaxial organic crystals at the two-dimensional limit, Nat. Commun. **10**, 756 (2019).

[17] V. I. Belinicher and B. I. Sturman, The photogalvanic effect in media lacking a center of symmetry, Sov. Phys. Usp. **23**, 199 (1980).

[18] S. D. Ganichev, H. Ketterl, W. Prettl, E. L. Ivchenko, and L. E. Vorobjev, Circular photogalvanic effect induced by monopolar spin orientation in p-GaAs/AlGaAs multiple-quantum wells, Appl. Phys. Lett. **77**, 3146 (2000).

[19] X. Tao, P. Jiang, H. Hao, X. Zheng, L. Zhang, and Z. Zeng, Pure spin current generation via photogalvanic effect with spatial inversion symmetry, Phys. Rev. B **102**, 081402 (2020).

[20] S. D. Ganichev and W. Prettl, Spin photocurrents in quantum wells, J. Phys. Condens. Matter **15**, R935 (2003).

[21] M. M. R. Moayed, F. Li, B. Beck, J. C. Schober, and C. Klinke, Anisotropic circular photogalvanic effect in colloidal tin sulfide nanosheets, Nanoscale **12**, 6256 (2020).

[22] Y. Xie, M. Chen, Z. Wu, Y. Hu, Y. Wang, J. Wang, and H. Guo, Two-Dimensional Photogalvanic Spin-Battery, Phys. Rev. Appl. **10**, 034005 (2018).

[23] M. Chen, K. Lee, J. Li, L. Cheng, Q. Wang, K. Cai, E. E. M. Chia, H. Cheng, and H. Yang, Anisotropic picosecond spin-photocurrent from Weyl semimetal WTe_2, Acs Nano **14**, 3539 (2020).

[24] R. von Baltz and W. Kraut, Theory of the bulk photovoltaic effect in pure crystals, Phys. Rev. B **23**, 5590 (1981).

[25] A. M. Glass, D. V. D. Linde, and T. J. Negran, High-voltage bulk photovoltaic effect and the photorefractive process in $LiNbO_3$, Appl. Phys. Lett. **25**, 233 (1974).

[26] A. M. Burger, R. Agarwal, A. Aprelev, E. Schruba, A. Gutierrez-Perez, V. M. Fridkin, and J. E. Spanier, Direct observation of shift and ballistic photovoltaic currents, Sci. Adv. **5**, eaau5588 (2019).

[27] Z. Ji, G. Liu, Z. Addison, W. Liu, P. Yu, H. Gao, Z. Liu, A. M. Rappe, C. L. Kane, E. J. Mele, and R. Agarwal, Spatially dispersive circular photogalvanic effect in a Weyl semimetal, Nat. Mater. **18**, 955 (2019).

[28] G. Osterhoudt, L. K. Diebel, M. Gray, X. Yang, J. Stanco, X. Huang, B. Shen, N. Ni, P. J. W. Moll, Y. Ran, and K. S. Burch, Colossal mid-infrared bulk photovoltaic effect in a type-I Weyl semimetal, Nat. Mater. **18**, 471 (2019).

[29] J. Quereda, T. S. Ghiasi, J. You, J. V. Den Brink, B. J. Van Wees, and C. H. V. Der Wal, Symmetry regimes for circular photocurrents in monolayer $MoSe_2$, Nat. Commun. **9**, 3346 (2018).

[30] M. Nakamura, S. Horiuchi, F. Kagawa, N. Ogawa, T. Kurumaji, Y. Tokura, and M. Kawasaki, Shift current photovoltaic effect in a ferroelectric charge-transfer complex, Nat. Commun. **8**, 281 (2017).

[31] J. E. Spanier, V. M. Fridkin, A. M. Rappe, A. R. Akbashev, A. Polemi, Y. Qi, Z. Gu, S. M. Young, C. J. Hawley, D. Imbrenda, G. Xiao, A. L. Bennett-Jackson, and C. L. Johnson, Power conversion efficiency exceeding the Shockley-Queisser limit in a ferroelectric insulator, Nat. Photonics **10**, 611 (2016).

[32] M. Dressel and T. Peterseim, Infrared investigations of the neutral-ionic phase transition in TTF-CA and its dynamics, Crystals **7**, 17 (2017).

[33] J. Li and P. M. Haney, Circular photogalvanic effect in organometal halide perovskite $CH_3NH_3PbI_3$, Appl. Phys. Lett. **109**, 193903 (2016).

[34] H. Zou, C. Zhang, H. Xue, Z. Wu, and Z. L. Wang, Boosting the solar cell efficiency by flexo-photovoltaic effect? ACS Nano **13**, 12259 (2019).

[35] S. Nadupalli, J. Kreisel, and T. Granzow, Increasing bulk photovoltaic current by strain tuning, Sci. Adv. **5**, eaau9199 (2019).

[36] B. I. Sturman and V. M. Fridkin, *The Photovoltaic and Photorefractive Effects in Noncentrosymmetryic Materials* (Gordon and Breach Science Publishers, Philadelphia, 1992).

[37] P. Zhao, H. Yang, J. Li, H. Jin, W. Wei, L. Yu, B. Huang, and Y. Dai, Design of new photovoltaic systems based on two-dimensional group-IV monochalcogenides for high performance solar cells, J. Mater. Chem. A **5**, 24145 (2017).

[38] Q. Wang, J. Li, Y. Liang, B. Wang, and Y. Nie, BX_1-BX_2 (X1, X2 = P, As, Sb) lateral heterostructure: Novel and efficient two-dimensional photovoltaic materials with ultra-high carrier mobilities, J. Mater. Chem. A **7**, 10684 (2019).

[39] V. I. Belinicher, E. L. Ivchenko, and B. I. Sturman, Kinetic theory of the displacement photovoltaic effect in piezoelectrics, Sov. Phys. JETP **56**, 359 (1982).

[40] T. Rangel, B. M. Fregoso, B. S. Mendoza, T. Morimoto, J. E. Moore, and J. B. Neaton, Large Bulk Photovoltaic Effect and Spontaneous Polarization of Single-Layer Monochalcogenides, Phys. Rev. Lett. **119**, 067402 (2017).

[41] S. M. Young and A. M. Rappe, First Principles Calculation of the Shift Current Photovoltaic Effect in Ferroelectrics, Phys. Rev. Lett. **109**, 116601 (2012).

[42] S. M. Young, F. Zheng, and A. M. Rappe, First-Principles Calculation of the Bulk Photovoltaic Effect in Bismuth Ferrite, Phys. Rev. Lett. **109**, 236601 (2012).

[43] T. Morimoto and N. Naoto Nagaosa, Topological nature of nonlinear optical effects in solids, Sci. Adv. **2**, e1501524 (2016).

[44] K. N. Okada, N. Ogawa, R. Yoshimi, A. Tsukazaki, K. S. Takahashi, M. Kawasaki, and Y. Tokura, Enhanced photogalvanic current in topological insulators via Fermi energy tuning, Phys. Rev. B **93**, 081403(R) (2016).

[45] E. J. Konig, H.-Y. Xie, D. A. Pesin, and A. Levchenko, Photogalvanic effect in Weyl semimetals, Phys. Rev. B **96**, 075123 (2017).

[46] V. M. Kovalev and I. G. Savenko, Photogalvanic currents in dynamically gapped transition metal dichalcogenide monolayers, Phys. Rev. B **99**, 075405 (2019).

[47] B. M. Fregoso, Bulk photovoltaic effects in the presence of a static electric field, Phys. Rev. B **100**, 064301 (2019).

[48] H. Soifer, A. Gauthier, A. F. Kemper, C. R. Rotundu, S.-L. Yang, H. Xiong, D. Lu, M. Hashimoto, P. S. Kirchmann, J. A. Sobota, and Z.-X. Shen, Band Resolved Imaging of Photocurrent in a Topological Insulator, Phys. Rev. Lett. **122**, 167401 (2019).

[49] A. Avdoshkin, V. Kozii, and J. E. Moore, Interactions Remove the Quantization of the Chiral Photocurrent at Weyl Points, Phys. Rev. Lett. **124**, 196603 (2020).

[50] Y. Gao, Y. Zhang, and D. Xiao, Tunable Layer Circular Photogalvanic Effect in Twisted Bilayers, Phys. Rev. Lett. **124**, 077401 (2020).

[51] S. V. Zhukovsky, V. E. Babicheva, A. B. Evlyukhin, I. E. Protsenko, A. V. Lavrinenko, and A. V. Uskov, Giant Photogalvanic Effect in Noncentrosymmetric Plasmonic Nanoparticles, Phys. Rev. X **4**, 031038 (2014).

[52] G. Kresse and J. Hafner, Ab Initio molecular dynamics for liquid metals, Phys. Rev. B: Condens. Matter **47**, 558 (1993).

[53] W. Kohn and L. J. Sham, Self-consistent equations including exchange and correlation effects, Phys. Rev. B **140**, 1133 (1965).

[54] Q. Wei and X. Peng, Superior mechanical flexibility of phosphorene and few-layer black phosphorus, Appl. Phys. Lett. **104**, 251915 (2014).

[55] W. Zhu, M. N. Yogeesh, S. Yang, S. H. Aldave, J.-S. Kim, S. Sonde, and D. Akinwande, Flexible black phosphorus ambipolar transistors, circuits and AM demodulator, Nano Lett. **15**, 1883 (2015).

[56] G. Wang, G. C. Loh, R. Pandey, and S. P. Karna, Out-of-plane structural flexibility of phosphorene, Nanotechnology **27**, 055701 (2016).

[57] J. P. Perdew, K. Burke, and M. Ernzerhof, Generalized Gradient Approximation Made Simple, Phys. Rev. Lett. **77**, 3865 (1996).

[58] H. J. Monkhorst and J. D. Pack, Special points for Brillouin-zone integrations, Phys. Rev. B **13**, 5188 (1976).

[59] L. E. Henrickson, Nonequilibrium photocurrent modeling in resonant tunneling photodetectors, J. Appl. Phys. **91**, 6273 (2002).

[60] J. Z. Chen, Y. B. Hu, and H. Guo, First-principles analysis of photocurrent in graphene PN junctions, Phys. Rev. B **85**, 155441 (2012).

[61] Y. Q. Xie, L. Zhang, Y. Zhu, L. Liu, and H. Guo, Photogalvanic effect in monolayer black phosphorus, Nanotechnology **26**, 455202 (2015).

[62] L. Zhang, K. Gong, J. Z. Chen, L. Liu, Y. Zhu, D. Xiao, and H. Guo, Generation and transport of valley-polarized current in transition-metal dichalcogenides, Phys. Rev. B **90**, 195428 (2014).

[63] J. Chen, L. W. Zhang, L. Zhang, X. L. Zheng, L. Xiao, S. Jia, and J. Wang, Photogalvanic effect induced fully spin polarized current and pure spin current in zigzag SiC nanoribbons, Phys. Chem. Chem. Phys. **20**, 26744 (2018).

[64] S. Datta, Linear-response formulation for mesoscopic systems with arbitrary interactions, Phys. Rev. B **46**, 9493 (1992).

[65] O. Madelung and H. J. Juretschke, *Introduction to Solid State Theory*, Springer Series in Solid-State Sciences Vol. 2 (Springer Verlag, Berlin, 1978).

[66] Y. Luo, Y. Hub, and Y. Xie, Highly polarization-sensitive, visible-blind and selfpowered ultraviolet photodetection based on two-dimensional wide bandgap semiconductors: A theoretical prediction, J. Mater. Chem. A **7**, 27503 (2019).

[67] T. Hong, B. Chamlagain, W. Lin, H.-J. Chuang, M. Pan, Z. Zhou, and Y.-Q. Xu, Polarized photocurrent response in black phosphorus field-effect transistors, Nanoscale **6**, 8978 (2014).

[68] J. Qiao, X. Kong, Z.-X. Hu, F. Yang, and W. Ji, High-mobility transport anisotropy and linear dichroism in few-layer black phosphorus, Nat. Commun. **5**, 4475 (2014).

[69] V. Tran and L. Yang, Scaling laws for the band gap and optical response of phosphorene nanoribbons, Phys. Rev. B **89**, 245407 (2014).

[70] T.-Y. Su, H. Medina, Y.-Z. Chen, S.-W. Wang, S.-S. Lee, Y.-C. Shih, C.-W. Chen, H. C. Kuo, F.-C. Chuang, and Y.-L. Chueh, Phase-engineered $PtSe_2$-layered films by a plasma-assisted selenization process toward all $PtSe_2$-based field effect transistor to highly sensitive, flexible, and wide-spectrum photoresponse photodetectors, Small **14**, 1800032 (2018).

[71] Q. Xiao, C.-X. Hu, H.-R. Wu, Y.-Y. Ren, X.-Y. Li, Q.-Q. Yang, G.-H. Dun, Z.-P. Huang, Y. Peng, F. Yan, Q. Wang, and H.-L. Zhang, Antimonene-based flexible photodetector, Nano Horiz. **5**, 124 (2020).

[72] L. Wang and C. Wang, Negative/zero thermal expansion in black phosphorus nanotubes, Phys. Chem. Chem. Phys. **20**, 28726 (2018).

[73] M. Inglot, V. K. Dugaev, J. Berakdar, and J. Barnaś, Light absorption and pseudospin density generation in graphene nanoribbons, Phys. Rev. B **100**, 165406 (2019).

[74] Q. Wu, L. Shen, Z. Bai, M. Zeng, M. Yang, Z. Huang, and Y. P. Feng, Efficient Spin Injection Into Graphene through a Tunnel Barrier: Overcoming the Spin-Conductance Mismatch, Phys. Rev. Appl. **2**, 044008 (2014).

[75] J. Kang, W. Liu, D. Sarkar, D. Jena, and K. Banerjee, Computational Study of Metal Contacts to Monolayer Transition-Metal Dichalcogenide Semiconductors, Phys. Rev. X **4**, 031005 (2014).

[76] M. Chen, Z. Yu, Y. Q. Xie, and Y. Wang, Spin-polarized quantum transport properties through flexible phosphorene, Appl. Phys. Lett. **109**, 142409 (2016).

[77] M. Chen, Z. Yu, Y. Wang, Y. Xie, J. Wang, and H. Guo, Nonequilibrium spin injection in monolayer black phosphorus, Phys. Chem. Chem. Phys. **18**, 1601 (2016).